Tight metal binding by humic acids and its role in biomineralization †

Geoffrey Davies,*,[a] Amjad Fataftah,[a] Aleksandr Cherkasskiy,[a] Elham A. Ghabbour,[b] Amal Radwan,[c] Susan A. Jansen,[d] Santha Kolla,[d] Mark D. Paciolla,[d] Lawrence T. Sein, Jr.,[d] Wolfgang Buermann,[e] Mahalingam Balasubramanian,[e] Joseph Budnick[e] and Baoshan Xing[f]

[a] Chemistry Department and the Barnett Institute, Northeastern University, Boston, MA 02115, USA
[b] Soil Salinity Laboratory, Agricultural Research Center, Bacos, Alexandria 21616, Egypt
[c] Chemical Engineering Department, Alexandria University, Alexandria, Egypt
[d] Chemistry Department, Temple University, Philadelphia, PA 19122, USA
[e] Physics Department, University of Connecticut, Storrs, CT 06269, USA
[f] Plant and Soil Science Department, University of Massachusetts, Amherst, MA 01003, USA

Analytical and thermodynamic data, EPR, FTIR, solution ^1H and solid-state ^{13}C cross polarization magic angle spinning NMR and solid-state extended X-ray absorption fine structure (EXAFS) and X-ray absorption near-edge structure (XANES) spectra have been recorded for purified humic acids (HAs) isolated from a German peat (GHA), an Irish peat (IHA), an unpolluted New Hampshire bog soil (NHA) and their tightly bound copper(II), iron(III) and manganese(II) forms. Brief water washing of partly or fully metal-loaded HAs leaves 'tightly' bound metal in the isolated freeze-dried solids. Most of this metal is removed by washing with 0.1 M HCl, indicating acidic HA functional groups as principal metal binding sites. The number of nearest-neighbour atoms co-ordinated to tightly bound Cu^{II} (four), Fe^{III} (six, probably with distorted geometry) and Mn^{II} (six, undistorted) in solid GHA, IHA and NHA were determined by XANES and EXAFS spectroscopy with reference standards. Isotherms measured at 20.0 °C and pH 2.4–3.2 with $[M]_{total} = 0.18–25.8$ mM for tight, reversible $Cu^{2+}(aq)$, $Fe^{3+}(aq)$, and $Mn^{2+}(aq)$ binding by solid IHA and NHA fit the Langmuir model and give the pH-independent stoichiometric site capacities v_i and equilibrium constants K_i for metal binding at specific HA sites $i = A$, B and C. Tight binding sites A, B and C of IHA are occupied by Cu^{II}, sites A and B by Fe^{III} and site A by Mn^{II}, while only identical metal binding site A in NHA is tight enough to resist metal removal by brief water washing. A new helical HA molecular model based on the empirical formula $C_{36}H_{30}N_2O_{15} \cdot xH_2O$ visualizes metal binding and the likely roles of HAs in biomineralization. Site A is suggested to be carboxylate, mixed ligands probably constitute site B, and site C is tentatively assigned as the interior of the HA helix. Binding free energies and EPR evidence suggest that $Cu^{2+}(aq)$, $Fe^{3+}(aq)$ and $Mn^{2+}(aq)$ rapidly transfer between specific HA binding sites. This affects rates of metal release and transfer to minerals.

The brown or black biopolymers in animals, plants, soils, sediments and water called humic substances (HSs) are one of the Earth's richest carbon reservoirs. They are multifunctional polymers with major environmental roles that include direct involvement in biomineralization. However, the Earth's surface and biomineralization are mysteries because the molecular structures of HSs are unknown. These mysteries are yielding to research on highly purified HSs and the prospects of understanding their roles in the carbon cycle, biomineralization and other life processes are improving.

Humic substances traditionally are classified by their aqueous solubility,[1] which is imperfect because of their inherent metal and mineral binding properties. Fulvic acids (FAs, $\langle M_w \rangle$ limit ca. 5 kDa), the babies of the HSs family, are soluble at all pH. They generally exist at low concentrations in natural waters, are surface active[2] and are hard to isolate and purify. Their light absorption controls UV penetration of surface waters that regulates phytoplankton populations and other aqueous phenomena. Humins (HUs), the deceased HSs family members, are insoluble at all pH. They are weaker sorbents and metal binders than FAs and humic acids (HAs), and are further along in the natural progression from live animals and plants towards 'dead' coals and carbon.[1]

Humic acids, the children and adults of the HSs family, are highly functionalized, carbon-rich biopolymers that are anchored in soil organic matter (SOM) by metal binding and attachment to clays and minerals.[3] Distinction of low $\langle M_w \rangle$ HAs from FAs is hard because polymer molar mass determinations (e.g. with gel permeation chromatography and viscosity measurements) are frustrated by the desire of HSs to aggregate.[1,4]

Humic acids are the Earth's sponges, thermal buffers and storehouses. As its primary water retainers, metal binders and sorbents, they regulate soils and sediments.[5,6] Their water retention gives the Earth thermal buffer capacity that prevents catastrophic climates. They are amorphous,[7] fractal materials[8–10] that have been modelled.[3,11–14]

Fig. 1(a) shows the lowest energy conformation *SRRSRRS* of the proposed Temple-Northeastern-Birmingham (TNB) HA building block $C_{36}H_{30}N_2O_{15} \cdot xH_2O$ ($x = 0–15$, water not shown) derived[12b] after allowance for polysaccharide and protein content from analytical data for HAs isolated with different methods from many soil sources and from modelling work.[12b,c] Its enantiomer *RSSRSSR* has the same lowest energy. Both enantiomers benefit from a favorable 3.6 Å van der Waals interaction between rings A and C in Fig. 1(a). Biosynthesis of this HA building block from phenylalanine and tryptophan has been rationalized.[12c] High-purity HAs are chiral and contain amide bonds.[12a] Fig. 1(b) predicts how the lowest-energy TNB HA building blocks link through amide ('peptide') bonds. The resulting helical secondary HA structure in Fig. 1(c) is hydrophobic at north and south, has acidic functional groups at east
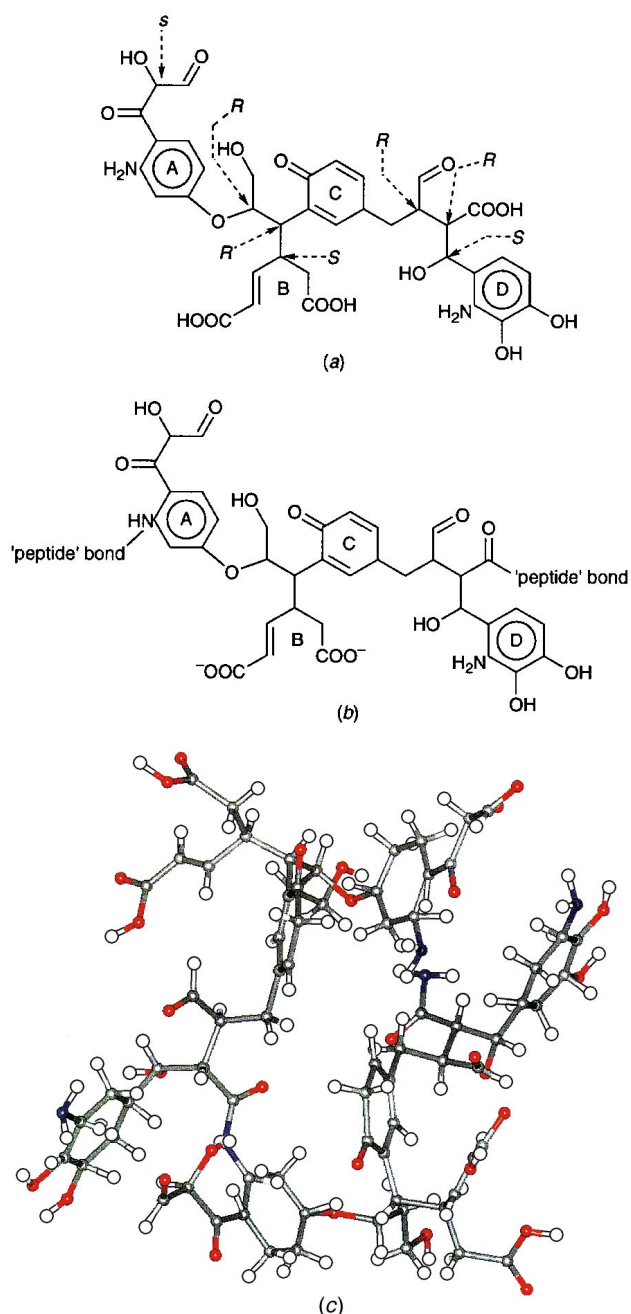
tiron®

Fig. 1 (*a*) Proposed biosynthetically generated TNB HA building block.[12b,c] This structure has seven chiral centres and 64 enantiomeric pairs, one of which has by far the lowest energy.[11,12] (*b*) Linkage of TNB to form HA. (*c*) One half turn of the resulting helix. Colour code: grey, carbon; red, oxygen; blue, nitrogen; white, hydrogen

and west, is lined with polar hydrophobic groups and has an elliptical cross-section. This secondary structure likely is terminated by amino acids or carbohydrates that always are found with HAs.[3] It has a central cavity for water, metal and solute binding. This water-filled, helical HA model[12] is consistent with many HA properties.[1–24]

Humic acid molecules extend at high pH because of their surface negative charge, but neutralization of their carboxylate and phenolate groups at lower pH causes aggregation to give aqueous gels that typically are 95–98% w/w water. The gels can be oven (O), freeze (F) or supercritical fluid CO_2 (SCF, after replacing their water with an organic liquid like acetone) dried to give solids with different morphologies (Fig. 2). The high-surface-area solid aerogel in Fig. 2(*c*) likely reflects the macroscopic framework of the original aqueous gel and those of waterlogged HAs in soils and sediments.[19]
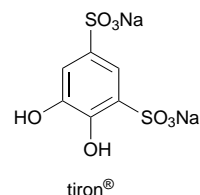
Reproducible data[22,23] for adsorption of 14 nucleic acid constituents (NACs) on a solid compost-derived HA and on solid HA particles from different soil sources without or with added Hg^{II}[24] show that HAs can be purified to the point where they become understandable. The data fit the Langmuir model for reversible solute adsorption in sequential steps labelled i = A, B and C.[14,22–24] Analysis gives the stoichiometric site capacity v_i and the equilibrium constant K_i for each solute and step. The v_i data indicate interaction of the HA surface with the nucleobase units of NAC solutes. Linear plots of log K_i *vs.* $1/T$ demonstrate interaction of a given solute with specific HA sites. Adsorption enthalpy and entropy data pairs (ΔH_i, ΔS_i) are linearly correlated for each solute and step, indicating that HAs are free-energy buffers.[14,22–24]

The absolute structures of HSs are unknown and the roles of HA-bound metals in soil/sediment C turnover, biomineralization and other life processes are unclear. However, metals have high potential as probes of humic acid structures. Humic acids can be demetallated and demineralized with Chelex® resins[25a] and aqueous tiron® (4,5-dihydroxybenzene-1,3-disulfonic acid, disodium salt).[26]

This paper reports analytical and thermodynamic data, EPR, Fourier-transform (FT) IR, solution ^{1}H and solid-state ^{13}C cross-polarization magic angle spinning (CP MAS) NMR spectra, and solid-state X-ray absorption near-edge structure (XANES) and extended X-ray absorption fine structure (EXAFS) spectra for purified HAs isolated from a German peat (GHA), an Irish peat (IHA), an unpolluted New Hampshire bog soil (NHA) and their tightly bound metal forms. A helical HA molecular model based on the empirical formula $C_{36}H_{30}N_2O_{15}\cdot xH_2O$[12b,c] visualizes metal binding and the likely roles of HAs in biomineralization.

Experimental

Materials

Humic acids. The Northeastern group has spent four years isolating, purifying, characterizing and comparing humic acids from composts, plants, peats, sediments and soils from different locations. We have found especially rich sources of HA samples IHA and NHA (Table 1): a peat from the Turf Board Company, Cork, Ireland and an unpolluted bog soil collected high in the White Mountain National Park in Rumney, New Hampshire, respectively. Humic acid GHA was isolated with the same protocol from a peat sample provided by Staatsbad Pyrmont AG, Bad Pyrmont, Germany.

Acids HCl, HF and HNO_3 and base NaOH were analytical reagent grade and doubly deionized water was employed throughout.

The HAs of this and our other research were isolated with the thorough, mild protocols of Scheffer *et al.*[28] and as modified by substitution of the first four Soxhlet source pre-extraction solvents (diethyl ether, acetone, ethanol and 1,4-dioxane)[28] with benzene–methanol (2:1 v/v),[29] and with added steps that remove structural polysaccharides[30] before aqueous base extraction and aqueous HA gel formation when the extracts are brought to pH 1.0 with concentrated HCl[16b] (Scheme 1).[28,29] We ensured that the HA product isolated from a given source with these methods is the same material. As-isolated HA samples were demetallated and demineralized by treatment with aqueous tiron® at pH 6.3 and there was no residual tiron®

Table 1 Analytical data for as-isolated, purified GHA, IHA and NHA

| Humic acid | % Yield[a] | Analysis[b] (%) | | | % Ash[c] | Total acidity[d] | RCO₂H[d] | Phenolic OH[d,e] |
		C	H	N				
GHA	29	50.51	5.32	1.71	1.5	7.9	3.2	4.6
IHA	43	50.46	5.56	2.06	0.89	12.4	3.3	9.2
NHA	50	52.90	5.40	2.00	0.25	8.4	2.7	5.7

[a] On a dry source weight basis. [b] On a dry, ash-free basis. [c] Determined by combustion of 100.0 mg HA samples in air at 850 °C for 2 h. [d] Units are mequivalents g⁻¹ HA. For methods see ref. 27. [e] Taken as the difference between columns 7 and 8 (see ref. 27).
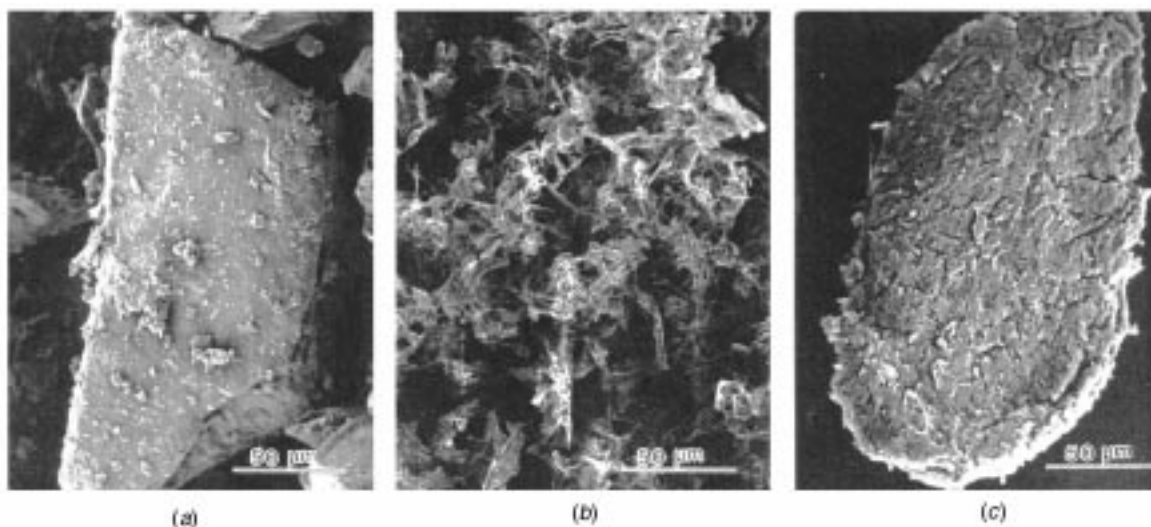
Fig. 2 Scanning electron micrographs of solids obtained by oven (*a*), freeze (*b*) and supercritical fluid CO_2 drying (*c*) of portions of the same aqueous HA gel

Scheme 1[28–30]
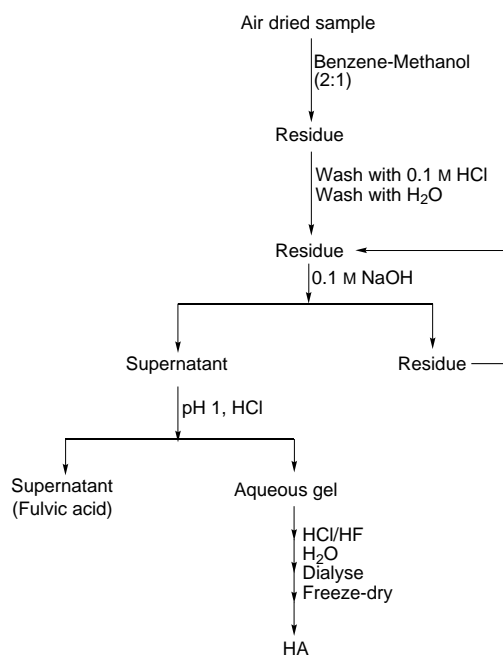
in the products.[26] We carefully compared our HA samples with each other, with compost-derived HAs and with International Humic Substances Society (IHSS) HA standards.

Humic acid characterization

Elemental and functional group analysis. The C, H and N contents of freeze-dried solids GHA, IHA and NHA were measured by Galbraith Laboratories, Knoxville, TN. The metal content of each freeze-dried as-isolated, metal-loaded acid-washed or metal-loaded water-washed HA sample was meas-

ured with a Leeman Laboratories PlasmaSpec inductively coupled plasma spectrometer fitted with a computer-controlled Echelle grating. Humic acid samples (25.0 mg) were boiled in HNO_3–$HClO_4$ (1:1 v/v, 20 cm³) until the volume was 2 cm³. After cooling, the solutions were adjusted to 25.0 cm³ in calibrated polycarbonate volumetric flasks prior to analysis. All measurements were calibrated with Spex reference solutions of the respective elements taking full account of matrix effects. The analytical wavelengths (nm) and detection limits (ppm) were as follows: Cu, 324.75, 0.0054; Fe, 238.24, 0.0046; Mn, 257.61, 0.0014. The total acidity and carboxylic acid contents of GHA, IHA and NHA were measured with reliable chemical methods.[27] Amino acid and carbohydrate contents of GHA, IHA and NHA were measured as previously described.[31]

FTIR and NMR characterization. Room-temperature KBr disc FTIR and solution-phase ^1H NMR spectra of GHA, IHA, NHA and their metal-loaded forms were measured with conventional techniques.[7] Solid-state ^{13}C NMR spectra identify and measure structural groups of SOM.[32–36] Conventional solid-state ^{13}C NMR spectroscopy with CP MAS (contact time 1 ms, recycle time 1 s)[33,34,36] was conducted on solid room-temperature samples of IHA and NHA with a Bruker AM 300 instrument at the University of Massachusetts and a Bruker AMX2-300 instrument at the University of Calgary. One set of conditions were 75.4 MHz frequency, 5 MHz spinning rate and a 90° pulse width of 5.5 µs. The Calgary measurements also employed a new pulse sequence (ramp CP, contact time 2.5 ms, recycle time 1 s).[37] Dipolar-dephasing CP MAS was used to differentiate non-protonated and protonated carbon. We calculated percentages of structural components with the procedures of Stevenson[33] and Chen and Pawluk.[36]

Metal sources. The copper(II) and manganese(II) sources were Fisher-certified ACS reagent grade $Cu(CH_3CO_2)_2 \cdot 2H_2O$ and $Mn(CH_3CO_2)_2 \cdot 4H_2O$, respectively. The iron(III) sources were

$FeNH_4(SO_4)_2 \cdot 12H_2O$ (Fisher-certified ACS reagent grade) and $Fe(CH_3CO_2)_2(OH) \cdot 4H_2O$. The latter empirical formula (M 263.0; 21.3% Fe^{III}, 21.3% Fe; calc. 21.2%) is that of the product of ambient air oxidation of solid $Fe(CH_3CO_2)_2$ (Alfa) over a 7 yr period in its opened vial. Each metal salt was dissolved in water adjusted with HNO_3 to pH 2.0 to avoid cation hydrolysis and polymerization, especially for iron(III). Each 0.100 M stock solution was stirred overnight at room temperature to ensure hydrolytic equilibrium and analysed for its respective metal. No stock solutions became cloudy or precipitated solids during the metal binding measurements.

Maximum metal capacities of humic acids. The maximum metal capacities of freeze-dried solids IHA and NHA were measured by shaking 100.0 mg of a given HA in 100.0 cm³ of each of the above metal stock solutions for 48 h at 20.0 °C and pH 2.0. Each solid product was separated by centrifugation, washed five times for 5.0 min with water by centrifugation and freeze dried in a Labconco lyophilizer. All the resulting solid samples were analysed by inductively coupled plasma emission spectroscopy as described above.

Washing of metal-loaded humic acids with 0.1 M HCl. Water-washed, partially dried, maximum metal-loaded humic acids were shaken with 0.1 M HCl for 24 h at 20.0 °C. The solid product was separated by centrifugation, washed five times for 5.0 min with water and then freeze dried and analysed for the desired metal as described above.

Tight-metal-binding isotherms. Tight-metal-binding isotherms were measured at pH 2.4–3.2 to avoid HA dissolution and metal cation polymerization. Aliquots (100.0 mg) of solid IHA or NHA were shaken for 48 h at 20.0 °C with solutions (100.0 cm³) of $[M]_{total}$ ranging from 0.18 to 25.8 mM. The treatment solutions were made by dilution of the respective stock solutions described above. Measurements of reactant mixtures after 48 h equilibration with solid HAs indicated a supernatant pH range of 2.4–3.2 with clear supernatants in all cases. Each solid product was collected by centrifugation, washed five times for 5.0 min with water, freeze dried and analysed for the desired metal as above. The data were used to calculate the amount of metal bound (A, mmol g⁻¹ HA) and the equilibrium metal ion concentration c (mM) for each metal binding step.

EPR measurements

The EPR spectra of solid HA–metal samples were measured with a Bruker ER200 X-band spectrometer at 75 K. This instrument is fitted with a Bruker ER035 gaussmeter with a minimum resolution of 0.1 G at a scan rate of 0.25 G s⁻¹ and with a Bruker ER201 frequency controller. Spectra were collected through an interfaced 486 MHz personal computer and simulated with theory based on a second-order perturbation effect.[38]

XANES and EXAFS measurements

Method. X-Ray absorption spectra of solid metal-loaded HA samples were collected on Beam Line X-11A at the National Synchrotron Light Source (NSLS) at Brookhaven National Laboratory, Upton, New York with a double Si(111) crystal monochromator. Higher harmonic reflections were selectively rejected by detuning the primary beam by 30–50%. K-Edge XAFS data were obtained for Cu, Fe and Mn at 77 K and room temperature. Highly concentrated samples and standards were measured in transition mode [$\ln(I_0/I)$], where I_0 and I were monitored with ionization chambers whose gas mixture was adjusted so that about 20% of the incident X-ray intensity I_0 and 80–90% of the transmitted intensity I were absorbed. Spectra for less concentrated samples were collected in the fluorescence mode (I_f/I_0) with a Lytle ionization detector of fluorescence intensity I_f. A Stern–Heald–Soller slit

assembly in conjunction with an appropriate filter reduced the elastic and Compton-scattered background components. Reference metal-foil spectra were measured simultaneously with each data set for energy calibration. The I_0 in the fluorescence data was corrected before comparison of XANES spectra. Multiple scans were averaged for each sample to improve the signal to noise ratio.

Data reduction. Data analysis was performed with programs based on the University of Washington EXAFS analysis package. Data reduction followed a standard procedure of pre- and post-edge background removal, energy-independent step normalization at the edge and extraction of the XAFS $\chi(k)$ function.[39] Data collected in the fluorescence mode were initially corrected for energy dependence of the incident intensity. The threshold energy was chosen at the first inflection point. After extraction of the XAFS function, the radial distribution function (RDF) about the central absorbing atom was obtained by Fourier transformation of the k^3-weighted data.[39] The RDFs are not phase-shift corrected and thus each peak is displaced toward shorter distances by $\alpha = 0.3$–0.5 Å from the actual crystallographic position, depending on the scattering atom. Preliminary data fitting was performed by non-linear least-squares analysis of the data.

HA modelling methods

Our HA modelling methods are described in detail elsewhere.[11,12] The computed structures in Figs. 1(c) and **15**–**17** were generated with HYPERCHEM™ software.

Results and Discussion

Depending on its history, a typical soil contains 0–20% w/w HSs on a dry weight basis.[1,5,6,16,17] Irish peat and 'young' New Hampshire bog soil are unusually rich sources of respective humic acid IHA and NHA. The three HAs of this study have C, H, N contents typical of purified HAs from land that has seen little or no agricultural or other human use (Table 1).[1,5,6,16,17] They have lower ash contents than IHSS standard HAs, which leave 2–3% w/w ash on combustion. The IHA sample is more acidic than GHA and NHA, as reflected by its higher total acidity and apparent[27] phenolic OH content. However, the carboxylic acid contents of GHA, IHA and NHA are not too different (Table 1).

As-isolated, purified GHA, IHA and NHA have very low metal contents, with Al, Ca, Fe and Si predominating (Table 2). The sums ΣM of the metals analysed are 64.9 µg metal g⁻¹ IHA and 18.2 µg metal g⁻¹ NHA. The mass ratio 64.9/18.2 = 3.6 : 1 equals the ratio of ash contents (0.89/0.25 = 3.6 : 1, Table 1), indicating that all the metals analysed in as-isolated IHA and NHA are mineral bound. This is consistent with negligible metal and zero ash contents of HAs that have been demineralized with tiron®,[26] and EPR spectra at 75 K of IHA and NHA in Fig. 3(a) and 3(b) characteristic of mineral- and zeolite-

Table 3 Amino acid contents[a] of GHA, IHA and NHA[31]

Amino acid	GHA	IHA	NHA
Asp	32.2	47.4	66.8
Glu	36.6	54.0	70.9
Ser	36.0	44.4	60.9
His	7.5	9.7	19.7
Gly	45.6	57.9	64.4
Thr	8.2	12.2	16.1
Arg	51.1	70.6	70.6
Tyr	11.0	15.1	14.8
Val	40.1	56.6	51.6
Met	5.7	8.6	8.2
Phe	15.2	21.6	22.2
Ileu	24.7	34.0	35.5
Leu	37.1	50.2	53.1
Lys	n.d.[b]	n.d.	n.d.
Total	351	482	555

[a] Units are μmol g^{-1} HA; data courtesy of Drs B. E. Watt and M. H. B. Hayes, Birmingham University. [b] n.d. = Not detected.

Table 4 Carbohydrate contents* of GHA, IHA and NHA[31]

Carbohydrate	GHA	IHA	NHA
Rhamnose	12.2	7.3	4.1
Fucose	1.1	0.8	1.5
Ribose	0.1	0.3	0.4
Arabinose	1.4	2.3	2.5
Xylose	18.2	7.8	5.3
Mannose	7.3	10.5	12.4
Galactose	10.9	11.4	10.9
Glucose	49.3	49.1	45.2
Total	100.5	89.5	82.3

* Units are mg g^{-1} HA; data courtesy of Drs. B. E. Watt and M. H. B. Hayes, Birmingham University.
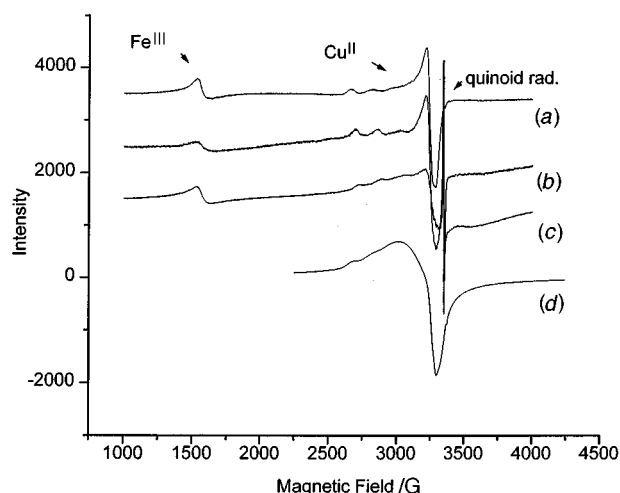

Fig. 3 The EPR spectra of HA samples at 75 K: (*a*) as-isolated freeze-dried solid IHA; (*b*) as-isolated freeze-dried solid NHA; (*c*) Fe^{III}-loaded, 0.1 M HCl-washed, water-washed, freeze-dried solid IHA; (*d*) Cu^{II}-loaded, water-washed, freeze-dried solid IHA. The following parameters apply to partly and maximally Cu^{II}-loaded GHA, IHA and NHA at 75 K; $g(x) = 2.1797$, $g(y) = 2.0596$, $g(z) = 2.3428$, $\langle g \rangle = 2.1940$, $A(x) = 29$, $A(y) = 31$, $A(z) = 138.6$, $\langle A \rangle = 65.8$ MHz

bound Fe^{III} and Cu^{II}.[25a] Thus, the tightest metal binding sites of HAs are in their associated minerals. Mineral-bound metals are difficult to remove with 0.1 M strong acid, Chelex® resins[25a] or tiron®.[26] Very weak peaks in the otherwise featureless X-ray powder spectra of GHA, IHA and NHA (not shown) indicate low levels of aluminosilicates in amorphous polymers.[7]

The amino acid and carbohydrate contents determined after strong acid hydrolysis of as-isolated samples GHA, IHA and NHA (Tables 3 and 4) were measured by Drs. B. E. Watt and
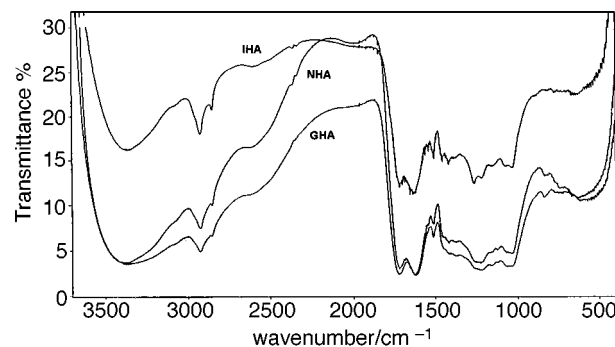

Fig. 4 Room-temperature KBr disc FTIR spectra of GHA, IHA and NHA

M. H. B. Hayes with the methods of ref. 31. Arginine, glutamic acid, glycine, valine, glucose, galactose, mannose and xylose predominate. The total measured amino acid and carbohydrate contents of GHA, IHA and NHA are similar and are too low to contribute significantly to their metal-binding properties.

Finding HAs with low metal, mineral, polysaccharide and protein contents (such as NHA, Tables 1–4) is a breakthrough because very tightly mineral-bound metals are not displaced when the same or other metals are added. Low-mineral-content HAs behave as if they were 'metal free' in terms of their capacities for a given metal.

Spectral properties

The room-temperature KBr disc FTIR spectra of GHA, IHA and NHA (Fig. 4) are very similar and have the following principal features: 2500 (broad, hydrogen-bonded pairs of CO$_2$H), 1715–1730 (C=O of carbonyl or CO$_2$H), 1630–1650 (asymmetric stretching of CO$_2^-$, aromatic C=C, C=O in CHO, C=O of quinones or in conjugation with alkenes), 1450–1460 (CH$_2$) and weak to medium bands in the 1030–1080 cm^{-1} region that are characteristic of HA.[40] The major effects of loading IHA, NHA and other purified HAs with Cu^{II} and other metals are loss of the 2500 and 1715–1730 cm^{-1} features, a shift to lower frequency and broadening of the doublet that includes the latter feature and minor changes in the region below 1500 cm^{-1}. These effects are consistent with metal binding by CO$_2^-$ functional groups, as concluded by others.[41–45] Washing metal-loaded GHA, IHA and NHA with 0.1 M HCl or demetallation and demineralization of as-isolated, purified HA samples with tiron® restores the features at 2500 and 1715–1730 cm^{-1},[26,46] which is expected if metals are bound by carboxylate functional groups in HA[41–45] and bridged by metals to each other and to minerals.[3,25,26,41–46]

Fig. 5 compares the room-temperature ^{1}H NMR spectra of GHA, IHA and NHA in 0.1 M NaOD–D$_2$O. The resonance at δ 4.8 is due to HOD and the peaks at δ 8.4 are due to polysaccharides.[47] The aromatic C–H resonance at δ 6.6–7.4 is well resolved, as expected for HAs with low paramagnetic ion content. Peaks centred at δ 3.8 are prominent and aliphatic peaks below δ 3.0 are well matched, indicating materials with very similar chemical constituents. Even lightly Cu^{II}-, Fe^{III}- and Mn^{II}-loaded GHA, IHA and NHA are much less soluble than the unloaded samples and low-intensity, broad, poorly resolved ^{1}H NMR spectra were observed in all cases.

Fig. 6 shows scanning electron micrographs of freeze-dried solids IHA and NHA and of solid NHA that had been loaded with an excess of completely dissolved Cu^{II} at pH 2.0, washed with water and freeze dried. The fibrous morphology of IHA and NHA is consolidated by metal loading to give the 'chunky' morphology [Fig. 6(*b*)] of vacuum oven-dried HAs.[7] This chunky morphology is the result of HA particle cross-linking by metals through functional group co-ordination or condensation of HA surface functional groups on removal of water by prolonged heating, respectively.[7,19,22]
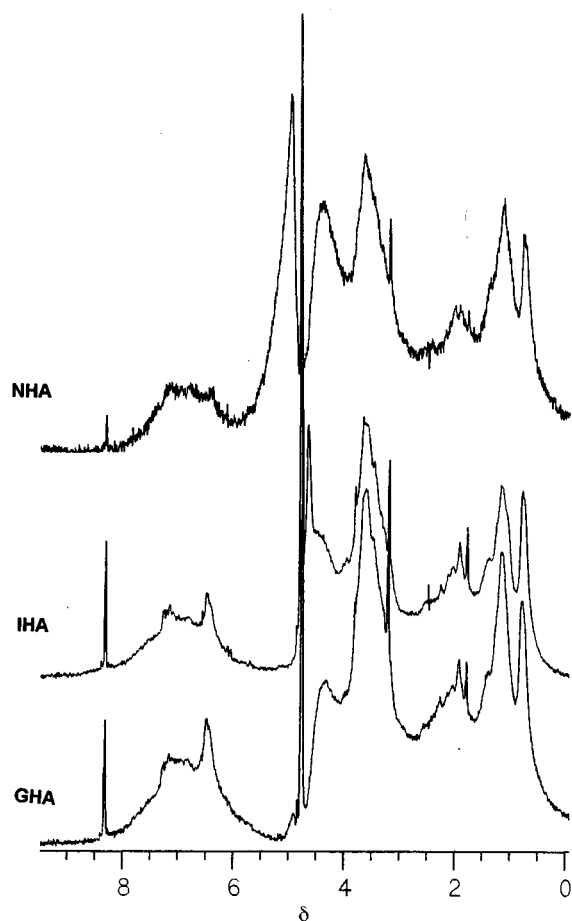
Fig. 5 Room-temperature ^{1}H NMR spectra of GHA, IHA and NHA in 0.1 M NaOD–D$_2$O

The ^{13}C CP MAS NMR spectra of solid IHA and NHA (Fig. 7) show that IHA and NHA are quite similar materials. Use of a new pulse sequence[37] improves spectral resolution of IHA, as found for other HS samples.[37] Applying the new pulse sequence[37] to IHA increases the apparent aromatic and carboxylic carbon contents and decreases the proportion of alkyl C, consistent with analytical data for IHA (Table 1). On average, 9% of the carbon in C$_{36}$H$_{30}$N$_2$O$_{15}$·xH$_2$O (or 3.2 CO$_2$H groups per formula unit) is carboxylic, in good agreement with the analytical data (Table 1). Further application of conventional[33,36] and improved[37] CP MAS pulse sequences to purified HAs samples will be helpful.

Metal-loading characteristics

We start with the reasonable assumption that HAs, as highly functionalized biopolymers, have inherent ability to bind metals.

Table 5 shows two sets of metal analytical data. The first (MIHA, MNHA) are the maximum metal capacities of IHA and NHA for Cu^{II}, Fe^{III} and Mn^{II}, respectively, from treatment with an excess of metal cations at 20.0 °C and pH 2.0, washing the solid products five times for 5.0 min with water, freeze drying and analysing the 'tight' metal-bound solid forms. The MIHA and MNHA data in Table 5 are orders of magnitude greater than those in Table 2, indicating organically bound metals that are not rapidly removed by water washing. The IHA tightly binds 1.1 (Mn^{II}) to 1.5 (Cu^{II}) times more metal than does NHA, and the ratio for tight iron(III) binding is 1.4:1. Humic acids from peats often have higher maximum metal capacities than those isolated from geologically younger soils and composts.[46]

Carboxylic acids are the most acidic HA functional groups.[1,5,6,16,27,32,33,46-48] Carboxylic acid group contents are reli-
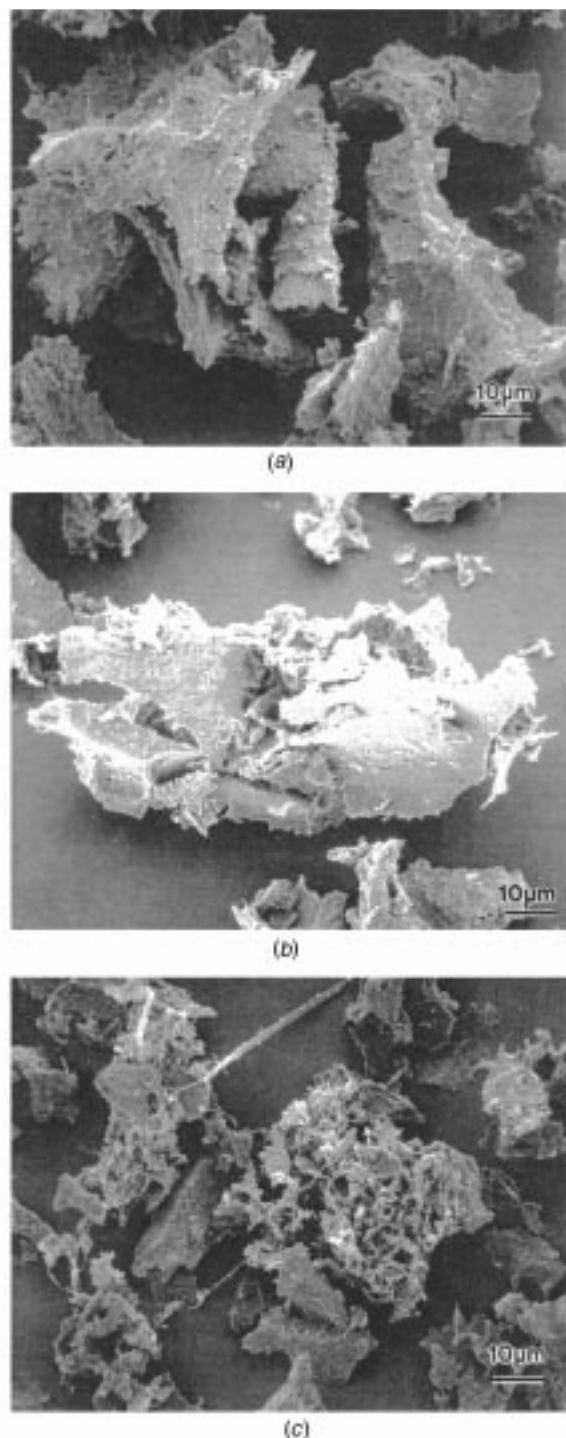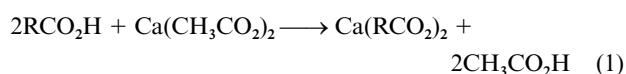

Fig. 6 Scanning electron micrographs of (a) IHA, (b) Cu-loaded NHA and (c) NHA, showing consolidation of the solid HA morphology by metal binding

ably measured by treating a known amount of HA with an excess of aqueous calcium acetate and titrating the resulting acetic acid from equation (1) with strong base.[27] Calcium

$$2RCO_2H + Ca(CH_3CO_2)_2 \longrightarrow Ca(RCO_2)_2 +$$
$$2CH_3CO_2H \quad (1)$$

analysis of the resulting water-washed, freeze-dried solids confirms that calcium is bound exclusively by ion-exchange reaction (1).[46]

Assuming that RCO$_2^-$ groups are principal organic binding sites for Cu^{II}, Fe^{III} and Mn^{II} in the pH range 2.0–3.2 of our experiments, the data in Tables 1 and 5 can be used to calculate the average number N of RCO$_2^-$ groups co-ordinated by each

Table 5 Metal analyses* of IHA and NHA after loading and washing with water and 0.1 M HCl
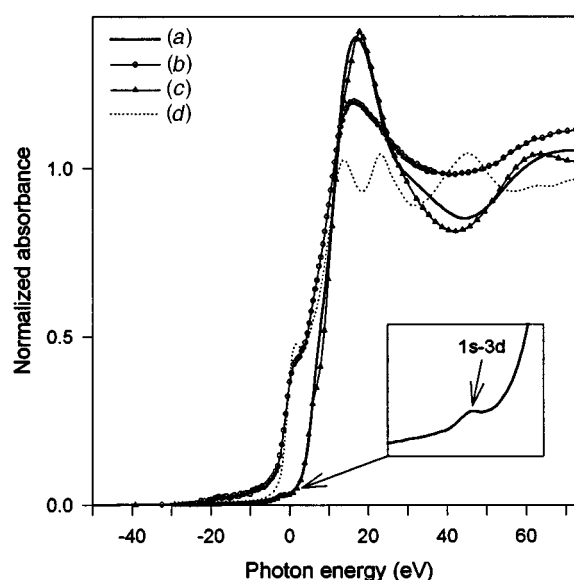
Metal	MIHA	N	MIHA + H$^+$	MNHA	N	MNHA + H$^+$
Cu	2.3	1.4	0.09	1.5	1.8	0.07
Fe	1.3	2.4	0.32	0.9	2.9	0.19
Mn	1.1	3.0	0.07	1.0	2.8	0.03

* Units are mmol g^{-1} HA.
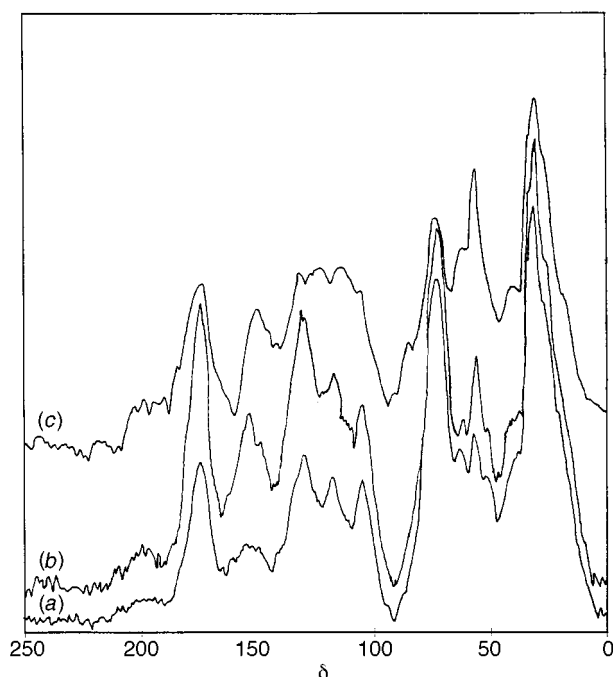
Fig. 7 Carbon-13 CP MAS NMR spectra of (*a,b*) IHA and (*c*) NHA. Assignments: δ 0–50, alkyl; 50–107, O-alkyl; 107–165, aromatic; 165–190, carboxyl; 190–220, carbonyl. Data (expressed as percentages of detected total carbon): IHA (conventional pulse sequence),[33] alkyl, 33.6; O-alkyl, 34.0; aromatic, 22.2; carboxyl, 8.4; carbonyl, 1.8; IHA (new pulse sequence),[37] alkyl, 27.0; O-alkyl, 29.3; aromatic, 30.9; carboxyl, 10.8; carbonyl, 1.9; NHA (conventional pulse sequence),[33] alkyl, 29.6; O-alkyl, 33.3; aromatic, 25.8; carboxyl, 9.2; carbonyl, 2.2

Fig. 8 The Cu-K edge spectra of (*a*) maximum Cu-loaded GHA; (*b*) residual Cu in GHA; (*c*) Cu$_2$(CH$_3$CO$_2$)·2H$_2$O and (*d*) copper foil. The first inflection point of the copper foil absorption edge is chosen as the zero point on the photon energy scale and corresponds to 8979 eV

metal centre. The results are shown in columns 3 and 6 of Table 5. We see that the six N estimates range from 1.4 to 3.0, with three of the values in the range 2.8–3.0. These are average values based on assumed carboxylate binding of Cu^{II}, Fe^{III} and Mn^{II} by IHA and NHA, as observed with Ca^{2+} [equation (1)].[46] The apparent phenol group contents of IHA and NHA differ by a factor of 2 (Table 1) but the N values are not sufficiently different to indicate any phenolate binding by Cu^{II}, Fe^{III} and Mn^{II} in the pH range 2.0–3.2.

The second data set (MIHA + H$^+$, MNHA + H$^+$) in Table 5 is the respective metal contents after washing each maximum metal-loaded HA with 0.1 M HCl for 24 h, then five times with water for 5 min, freeze drying and analysis of the resulting solid. The amount of bound metal remaining after this treatment ranges from 3–4% (Mn^{II} leached from MnNHA, Cu^{II} from CuIHA) to 21–24% (Fe^{III} from FeIHA and FeNHA) (Table 5, columns 4 and 7). Senesi and Calderoni[41] reported 42% w/w residual Fe, 15% residual Cu^{II} and 0.4% residual Mn^{II} on similar treatment of HAs from unamended and amended loam soil that was independent of the amendment time span. They concluded from these data that the binding affinity of these HAs decreases with M = Fe^{III} > Cu^{II} ≫ Mn^{II}. However, the data actually refer to the rates of acid-catalysed metal release from protonatable HA functional groups and not to the thermodynamic affinity of our and their HAs for metals, as indicated by equilibrium metal-binding constants (see below).

The simplest explanation of the data in columns 4 and 7 of Table 5 is that the tightest mineral metal-binding sites **M** of

as-isolated IHA and NHA are only partly filled, that the **M** sites can be depleted of Cu^{II} and Mn^{II} by washing with 0.1 M HCl and that the **M** site capacities of IHA and NHA are about 0.32 and 0.19 mmol g^{-1}, respectively. The EPR spectrum [Fig. 3(*c*)] of Fe^{III}-loaded IHA that had been washed with 0.1 M HCl, then five times with water, freeze dried and analysed indicates the presence of mineral-bound Cu^{II} and Fe^{III},[25] consistent with tightest metal binding by mineral sites **M**.

Metal-binding information from XAFS measurements

It is usual to focus in XANES studies on energy shifts of absorption edges and particular features to learn about an element's oxidation state and chemical environment. Fig. 8 is a XANES comparison of Cu in GHA, copper(II) acetate and copper foil. The residual copper in the as-isolated GHA was 0.9 μmol g^{-1} GHA (Table 2). Loading of as-isolated GHA with an excess of aqueous copper(II) acetate and washing with water gives a copper concentration of 2.3 mmol g^{-1} GHA (Table 5). Clear distinction of a difference between an excess of Cu-loaded GHA and residual Cu in GHA is apparent from the significant energy shift of the Cu-K absorption edge position. Fig. 8 indicates that Cu in the excess Cu-loaded GHA has a higher oxidation state than the residual Cu in GHA.

The XANES spectra of maximum Cu-loaded GHA, IHA and NHA and partly Cu-loaded GHA are indistinguishable. The data for maximum Cu-loaded GHA and copper(II) acetate are consistent with edge positions of copper(II) systems.[49,50] However, the XANES spectra of these two systems indicate different chemical environments of Cu. The small pre-edge peak observed in the maximum Cu-loaded GHA (Fig. 8, inset) and copper(II) acetate is usually described as a quadrupolar 1s–3d transition, which is facilitated by p–d mixing.[51] Absence of this peak and the significant shift toward lower energy of the edge position for residual Cu indicates a copper oxidation state
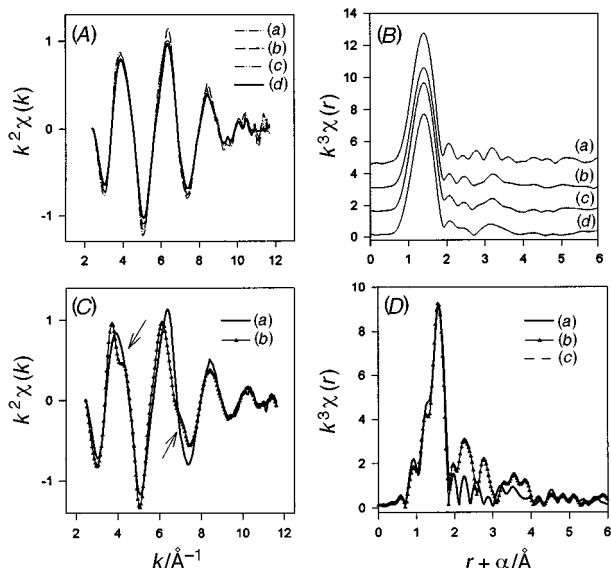
Fig. 9 (*A*) k^2-Weighted EXAFS comparison of (*a*) partly Cu-loaded GHA and maximum-Cu loaded (*b*) GHA; (*c*) NHA and (*d*) IHA at room temperature. (*B*) k^3-Weighted experimental Fourier transforms of the data in (*A*) (*k* range: 2.7–11.5 Å^{-1}). (*C*) k^2-Weighted EXAFS comparison of (*a*) maximum Cu-loaded GHA and (*b*) Cu$_2$(CH$_3$CO$_2$)$_4$·2H$_2$O at 77 K. (*D*) k^3-Weighted (*a, b*) experimental and (*c*) theoretical Fourier transforms of the data in (*C*) (extended *k* range: 2.7–14.5 Å^{-1}). The RDFs are not phase-shift corrected
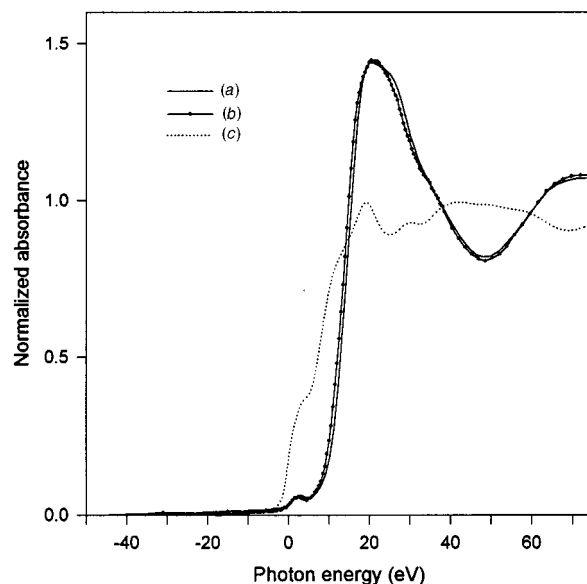

Fig. 10 The Fe-K edge spectra of (*a*) maximum Fe^{III}-loaded GHA; (*b*) residual iron in GHA and (*c*) iron foil. The first inflection point of the iron foil absorption edge is chosen as the zero point on the photon energy scale and corresponds to 7112 eV

of less than π. The shoulder seen at half step height for residual Cu in GHA is for a 1s–4p dipole transition. In well defined copper(I) states like Cu$_2$O, atomic-like transitions are distinct due to localized valence electrons. The extra ionic charge induced by neighbouring atoms in this case may shift atomic transition energies compared to those of the free copper ion. This effect is generally referred to as screening.[49] In metallic and strongly covalent copper materials screening effects are enhanced through strong hybridization, resulting in a broadening of the electron bands.[49] Broadening might explain the weak 1s–4p transition observed in the XANES of the residual Cu in GHA. Thus, the residual Cu appears to be bound to its remaining minerals. The correlation noted earlier between residual metal concentration and ash content in IHA and NHA and EPR evidence [Fig. 3(*a*)–3(*c*)] confirm that residual Cu in HAs is mineral-bound.

Fig. 9(*A*) and 9(*B*) show the k^2-weighted EXAFS spectra of maximum Cu-loaded GHA, IHA and NHA and their k^3-weighted Fourier transforms along with the spectrum of partly Cu-loaded GHA (concentration 4% w/w). The EXAFS spectra of the maximum Cu-loaded HAs and partly Cu-loaded GHA have identical primary frequency oscillations. Also striking is that high-frequency oscillations are not easily observed.

The Fourier-transformed EXAFS functions of the Cu-loaded HAs [Fig. 9(*B*)] show that the first co-ordination shell is located at the same position relative to the absorbing Cu atoms. The first-shell peak-area intensities vary only slightly, indicating no significant difference of the types and number of nearest-neighbour atoms. No high-*Z* backscatterers are evident beyond the first co-ordination shell. The weak scattering contribution from low-*Z* elements beyond the first shell to the EXAFS, seen as minor Fourier peaks, prevents a more detailed analysis. Thus, it is not possible to report differences in higher-order low-*Z* atomic environments in GHA, IHA and NHA. Also, EXAFS cannot confirm the existence of more than one copper binding site in HAs that is indicated by metal-binding isotherms (see below).

The FTIR data support carboxylate-bound Cu^{II} in HAs. The EXAFS spectrum of dimeric Cu$_2$(CH$_3$CO$_2$)$_4$·2H$_2$O, in which

each Cu atom is linked to four η^1:η^2-bridging carboxylate groups, was collected for comparison.

Fig. 9(*C*) shows the k^2-weighted EXAFS spectra of maximum Cu-loaded GHA and Cu$_2$(CH$_3$CO$_2$)$_4$·2H$_2$O. The spectra have clear differences. The primary low-frequency EXAFS contributions are similar, but the high-frequency oscillations for Cu$_2$(CH$_3$CO$_2$)$_4$·2H$_2$O indicated by arrows allow a visible distinction of the local atomic environments. In Cu$_2$(CH$_3$CO$_2$)$_4$·2H$_2$O the first-shell sinusoidal single-frequency EXAFS contribution is due to one Cu atom surrounded by 4 O at 1.97 Å.[52] The Cu–Cu interaction at 2.64 Å provides the second higher-frequency EXAFS contribution.

Fig. 9(*D*) compares the k^3-weighted experimental Fourier transforms of Cu$_2$(CH$_3$CO$_2$)$_4$·2H$_2$O and Cu in GHA. The data are not phase-shift corrected. The positions and intensities of the first-shell peaks in the FT overlap, indicating similar first-shell atomic environments. Preliminary fitting analysis with theoretical standards using FEFF6 and FEFFIT EXAFS software[53] confirms this result and assigns the first shell as 4 O or N atoms at 1.97 ± 0.02 Å away from Cu.[52] Distinct differences of these two systems are evident at greater distances from the copper absorber. For Cu$_2$(CH$_3$CO$_2$)$_4$·2H$_2$O the intense Fourier peak at 2.3 Å indicates the presence of a Cu atom at a distance of 2.64 Å, as confirmed by agreement of the experimental and theoretical spectra [Fig. 9(*D*)]. In contrast, no high-*Z* elements beyond the first shell of Cu-loaded GHA can be detected. Thus, no metal clustering, coprecipitation or polymerization effects are observable for Cu-loaded GHA. The EXAFS similarities of nearest-neighbour atoms in CuGHA and Cu$_2$(CH$_3$CO$_2$)$_4$·2H$_2$O support FTIR evidence that Cu atoms are co-ordinated by carboxylate functional groups of HAs.[41–46]

Fig. 10 shows Fe-K edge XANES spectra of maximum Fe^{III}-loaded and residual iron in GHA. Controlled loading with iron(III) gave 1.3 mmol Fe^{III} g^{-1} GHA, whereas the residual iron concentration of GHA is 5.3 μmol g^{-1} GHA (Table 2). Minor differences in the XANES spectra of these two systems are detectable. A 0.5 eV shift of the edge position toward higher energy of the maximum Fe^{III}-loaded GHA is observed, with slight differences of slopes beyond the absorption edge. The XANES spectra of Fe^{III}-loaded GHA, IHA and NHA are indistinguishable. The absorption edge positions of residual and maximum Fe-loaded GHA are those expected for iron(III) compounds. The XANES spectra have a small pre-edge peak assigned to a quadrupolar 1s–3d transition.[54] The location and

Table 6 The EXAFS parameters for copper(II) acetate and Cu^{II}-, Fe^{III}- and Mn^{II}-loaded GHA, IHA and NHA[a]

N^b	Atom	r/Å	$10^3\sigma^{2c}$/Å^2
4	Cu–O	1.97(2)	3.6
1	Cu–Cu	2.64(3)	5.8
4	Cu–X^d	1.97(2)	3.2
6	Fe–X^d	2.01(5)	7.0
6	Mn–X^d	2.20(4)	6.4

[a] The first two entries are for the copper(II) acetate reference. [b] Typical error is ±10%. [c] Debye–Waller factor at 77 K. [d] X = O or N.
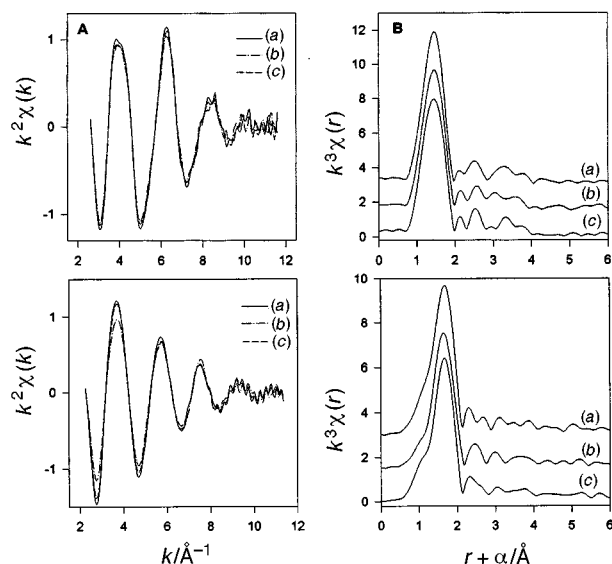

Fig. 11 (*A*) k^2-Weighted EXAFS comparison of maximum Fe^{III}-loaded (*a*) GHA, (*b*) NHA and (*c*) IHA at room temperature. (*B*) k^3-Weighted experimental Fourier transforms of the data in (*A*) (*k* range: 2.7–11.5 Å^{-1}). (*C*) k^2-Weighted EXAFS comparison of maximum Mn-loaded (*a*) GHA, (*b*) NHA and (*c*) IHA at room temperature. (*D*) k^3-Weighted experimental Fourier transforms of the data in (*C*) (*k* range: 2.7–11.0 Å^{-1}). The RDFs are not phase-shift corrected

Fig. 12 The EPR spectra of solid maximum Mn^{II}-loaded GHA, IHA and NHA at 75 K. Parameters: $\langle g \rangle$ = 2.0188, $\langle A \rangle$ = 119.0 MHz

area of this peak are very sensitive to co-ordination symmetry.[54] Further analysis of this particular transition might yield information on the geometries of the first atomic shell. As concluded for Cu, residual Fe^{III} in GHA appears to be mineral-bound.

Fig. 11(*A*) compares the k^2-weighted EXAFS spectra of maximum Fe-loaded GHA, IHA and NHA (the concentration range is 5–9% w/w). The EXAFS oscillations of the three systems are indistinguishable and no high-frequency oscillations are apparent. Fig. 11(*B*) shows the corresponding k^3-weighted experimental FT. In all three systems the first maximum in the FT peak is at the same position, with very little area-intensity variation. The first-shell atomic environment in the three Fe^{III}-loaded HAs appears identical. As seen for Cu-loaded HAs, no significant backscatterer beyond the first shell is discernible. The weak EXAFS signals from more distant shells, seen as low-intensity Fourier peaks, do not allow a clear distinction of a higher-order low-Z environment. As a result, the presence of more than one iron(III) binding site in HAs cannot be confirmed by EXAFS. As found for Cu^{II}, there is no evidence for iron clustering, coprecipitation or polymerization in Fe^{III}-loaded GHA, IHA or NHA.

Preliminary first-shell fitting with FEFF6 theoretical standards[53] was performed. The average Fe–O distance reported for α-Fe$_2$O$_3$ was employed to model the first-shell atomic environment.[53] The fit results indicate that Fe^{III} in HA is surrounded by 6 O or N atoms located at an average distance of 2.01 ± 0.05 Å. The nearest-neighbour distance range (Table 6) suggests iron(III) occupation of slightly different crystallographic sites that needs to be confirmed.
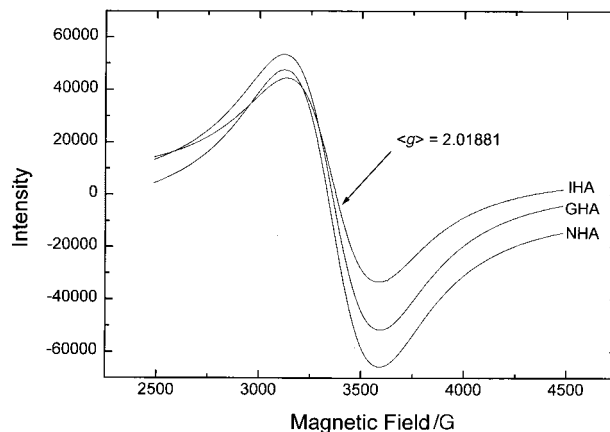
Fig. 11(*C*) shows the k^2-weighted EXAFS functions of maximum Mn-loaded GHA, IHA and NHA. The EXAFS phase functions of the three systems are exactly alike. Small differences in the EXAFS amplitudes are visible. No high-frequency beating can be seen. Fig. 11(*D*) shows the corresponding k^3-weighted experimental FT of the three maximum Mn^{II}-loaded HAs. As seen for Cu and Fe, the distance from the manganese absorber to the first atomic shell coincides in the three HAs, as indicated by the location of the first FT maxima. Absence of significant backscattering beyond the first shell resembles the situation for Cu^{II} and Fe^{III}. Differences in the Fourier peaks corresponding to higher-order shells are within the noise level. Preliminary fitting of the Mn-loaded HAs data was based on possible binding to HA carboxylate functional groups with the first-shell distance of manganese(II) acetate.[55] The fits show the Mn atom surrounded by 6 O or N atoms at a distance of 2.20 Å. The good-quality data fit for maximum Mn^{II}-loaded HAs indicates very little distortion of the first-shell distances, in contrast to the situation for Fe^{III} (see above and Table 6). The EPR spectra at 75 K in Fig. 12 confirm that manganese(II) centres in GHA, IHA and NHA are indistinguishable.[44]

Table 6 summarizes the numbers of nearest-neighbour atoms and their distances from the respective metal centres in Cu(CH$_3$CO$_2$)$_2$·2H$_2$O and Cu^{II}-, Fe^{III}- and Mn^{II}-loaded humic acids GHA, IHA and NHA. The relatively large uncertainties in first-shell Fe^{III}–X and Mn^{II}–X distances are ascribed to local geometric distortion of Fe^{III} and relatively weak manganese(II) binding, respectively.

Tight binding of metals by humic acids

Purified GHA, IHA and NHA are analytically comparable materials that bind Cu^{II}, Fe^{III} and Mn^{II} at similar sites with no change in oxidation state. Metal-binding measurements were made at low pH to avoid GHA, IHA and NHA dissolution and hydrolysis, polymerization and precipitation of the metal source and treatment solutions, especially in the case of iron(III).[56] We used two different sources of Fe^{III}, prepared the metal source and treatment solutions at pH 2.0 and monitored them for any significant change during the metal-binding measurements. Adding these solutions to solid HAs gave mixtures with pH 2.4–3.2 in which the HAs had negligible solubility with no evidence for redox reactions, metal polymerization-precipitation or significant pH changes at 20.0 °C in the 48 h equilibration time. The predominant aqueous metal species under our conditions are Cu^{2+}(aq), Fe^{3+}(aq) and Mn^{2+}(aq).[57]

Adding metal cations to a solid 'metal- and mineral-free' HA that has different organic binding sites *i* will fill the tightest binding sites first and metals in these sites will be the last to leave on washing the samples with water or strong acid. When the loaded HA is washed with water, any loosely held metal is
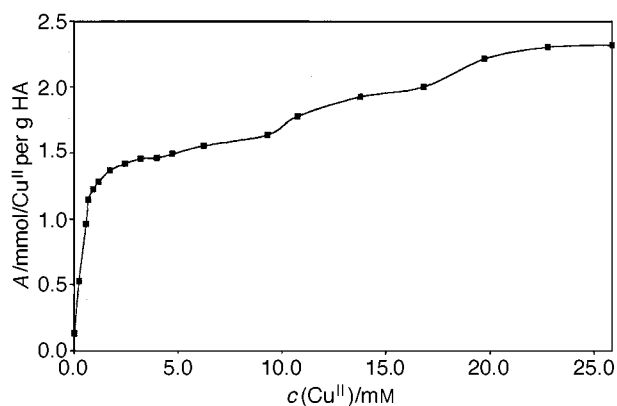
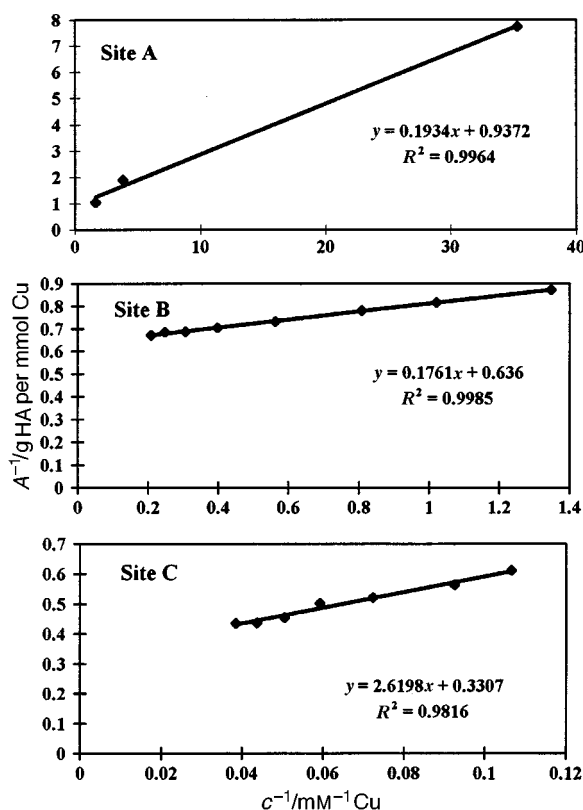**Fig. 13** Tight Cu^{II}-IHA loading isotherm at 20.0 °C and pH 2.4–3.2

Fig. 14 Plots of equation (5) for the data in Fig. 13

removed and only 'tightly' bound metal remains. The situation is more easily understood than when FAs and HAs are titrated with cations because interpretation of titration results is subject to Donnan effects and other complicated phenomena expected for polyelectrolytes.[58–60]

Reversible reaction of a metal cation M^{n+} with site i in a solid HA, equation (2), has equilibrium constant K_i, equation (3). If

$$M^{n+} + (HA\ site\ i)(s) \underset{}{\overset{K_i}{\rightleftharpoons}} M\text{–}(HA\ site\ i)(s) \qquad (2)$$
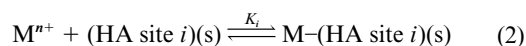
$$K_i = k_f/k_{r,i} \qquad (3)$$

metal binding by HAs is dissociatively controlled,[61] the rate constant k_f is characteristic of M^{n+} in all the equilibria. The presence of bound metal after water washing of a metal-loaded HA thus depends on small magnitudes of $k_{r,i}$ in equation (3), which determine the rates of metal loss from tight HA binding sites. When $k_{r,i}$ are small enough, the loading curve for a metal-loaded HA that has been washed with water (Fig. 13) is an isotherm that records the interaction of site i with sufficient excess of M^{n+} also to occupy weaker metal-binding sites.

The amount of metal A_A (mmol g^{-1}) bound at a specific HA site A is described by Langmuir equation (4). Here, K_A (M^{-1}) is

$$A_A = K_A v_A c/(1 + K_A c) \qquad (4)$$

the metal-binding equilibrium constant and v_A (mmol g^{-1}) is the stoichiometric capacity of site A for the particular metal cation. The equilibrium metal concentration c is calculated from A_A, as measured by metal analysis of the washed solid isolated after treatment of an HA with a solution of known volume and total metal concentration. Depending on the magnitude of K_A, equation (4) predicts that a plot of A_A vs. c (the isotherm) will curve toward the c axis with increasing c. Such curvature (as in Fig. 13) indicates specific metal binding by HA.[14,20–24]

Langmuir metal binding at specific HA site A predicts a linear plot of $1/A_A$ vs. $1/c$, equation (5), and K_A and v_A can be

$$1/A_A = (1/v_A) + (1/K_A v_A c) \qquad (5)$$

calculated from the intercept and slope.[14,22–24] The existence of equilibria (2) and the validity of equation (4) are indicated by positive intercepts $1/v_i$ ($i = A, B \ldots$) in linear segments of plots of equation (5) (Fig. 14).[14,22–24]

Fig. 13 shows the isotherm for tight copper(II) binding by IHA at 20.0 °C. The data were independent of pH in the range 2.4–3.2. Binding by organic groups in IHA occurs in three steps with increasing c, as indicated by linear plots of equation (5) for isotherm segments of the same data (Fig. 14). Stoichiometric site capacities v_i and equilibrium constants K_i were calculated from the slope and intercept of each segment. We tested all the isotherms with equation (5) to find if the data fit the model [equation (2)], the number of binding steps i with increasing c from the number of distinguishable linear segments, and v_i and K_i (at 20.0 °C and pH 2.4–3.2) for each step. All the isotherms gave linear or segmental linear plots of equation (5). The tight-binding isotherms for Cu^{II}, Fe^{III} and Mn^{II} were independent of pH from 2.4 to 3.2 and the source of iron(III), indicating interacting species Cu^{2+}(aq), Fe^{3+}(aq) and Mn^{2+}(aq), respectively.[57]

Tight metal-binding parameters

Tight HA metal-binding isotherm parameters at 20.0 °C and pH 2.4–3.2 are collected in Table 7. The ion Cu^{2+}(aq) tightly binds to IHA in three steps labelled A, B and C (Fig. 14), while only two steps are detected for Fe^{3+}(aq) and only one for Mn^{2+}(aq) binding by IHA and NHA.

The stoichiometric site-capacity data v_i in Table 7 indicate the following. (1) Since $v_A = 1.1 \pm 0.1$ mmol g^{-1} IHA is the same for binding of Cu^{2+}(aq), Fe^{3+}(aq) and Mn^{2+}(aq) at site A in IHA, then it must be the same binding site for these three metals. (2) Since $v_B = 1,.6 \pm 0.1$ mmol g^{-1} IHA is the same for Cu^{2+}(aq) and Fe^{3+}(aq) binding, site B of IHA is used for binding both of these cations. (3) $v_A < v_B < v_C$ for NAC adsorption on compost-derived HA (CHA), German peat-derived HA and Hg^{II}-loaded German peat-derived HA,[22–24] and for Cu^{2+}(aq) and Fe^{3+}(aq) binding by IHA (Table 7). However, Table 1 of ref. 14 shows that $\Sigma v_i = v_A + v_B + v_C$ for NAC adsorption ranges from 0.29 to 0.68 mmol solute g^{-1} CHA except for adsorption of adenine ($\Sigma v_i = 5.96$ mmol g^{-1} CHA) and cytosine ($\Sigma v_i = 3.37$ mmol g^{-1} CHA). With these exceptions, v_i and Σv_i for metal binding in Table 7 are much larger than for NAC solutes.[14,22–24] As expected, small metal cations bind at HA sites that are inaccessible to much larger NAC solute molecules and ions. (4) The sum of the site capacities is $\Sigma v_i = v_A + v_B + v_C = 5.6, 2.7$ and 1.2 mmol metal g^{-1} IHA (all ± 0.1 mmol metal g^{-1} IHA) for Cu^{2+}(aq), Fe^{3+}(aq) and Mn^{2+}(aq) binding by IHA, respectively, and $v_A = 1.1 \pm 0.1$ mmol metal g^{-1} NHA for tight binding of the respective cations on NHA. The total site capacity of IHA is larger than the measured maximum metal capacity MIHA in Table 5 for reasons explained below.

Table 7 Tight-binding isotherm parameters at 20.0 °C and pH 2.4–3.2

	IHA			NHA		
Metal	$v_i{}^a$	$10^{-3}K_i{}^b$	$-\Delta G_i{}^c$	$v_i{}^a$	$10^{-3}K_i{}^b$	$-\Delta G_i{}^c$
Cu^{II}						
A	1.1	4.9	5.0	1.3	4.8	4.9
B	1.6	3.6	4.8			
C	3.0	0.13	2.8			
Fe^{III}						
A	1.1	1.6	4.3	1.0	1.2	4.1
B	1.6	0.15	2.9			
Mn^{II}						
A	1.2	0.7	3.8	1.0	0.8	3.9

^{a} Units are mmol g^{-1} HA. Typical error is ±0.1 mmol g^{-1} HA. ^{b} Units are M^{-1}. Typical error is ±10%. ^{c} Units are kcal mol^{-1}.

Senesi and Calderoni[41] loaded a paleosol-derived HA from southern Italy with Cu^{II}, Fe^{III} and Mn^{II}, analysed the products and examined their EPR spectra. The HA contained appreciable amounts of Cu^{II} and Fe^{III} before loading. They concluded that oxygen-containing groups bind square-planar Cu^{II} but could not distinguish between four- and six-co-ordinated Fe^{III}. Binding affinity was concluded to decrease in the order $Fe^{III} > Cu^{II} \gg Mn^{II}$, which disagrees with our equilibrium data for low-metal-content IHA and NHA (Table 7). This same order was concluded for HAs isolated from an unamended and amended loam soil regardless of their origin.[42] Senesi and co-workers[41,42] conclusion is based on relative metal release rates, not on thermodynamic considerations. Table 5 (columns 4 and 7) shows that Fe^{III} is the last metal to leave acid-washed, metal-loaded IHA and MHA, as found by Senesi and co-workers.[41,42]

At least three iron(III) binding sites (with at least one octahedral) were assigned in an EPR and Mössbauer study of HAs and FAs with and without various chemical treatments.[43] Data for removal of Fe from a 27% ash content HA isolated from a Maine farm soil with tiron® indicate that three kinds of iron are present. One is mineral bound, one is stoichiometrically removed by tiron® and the third is competitively removed by tiron®.[26,46] McBride[44] concluded from EPR measurements that Mn^{II} interacts ionically with a mineral soil-derived HA, while Cu^{II} and $V^{IV}O$ are complexed by oxygen-containing groups.[45]

The equilibrium constants K_i for tight $Cu^{2+}(aq)$, $Fe^{3+}(aq)$ and $Mn^{2+}(aq)$ binding by IHA and NHA in Table 7 indicate the following. (1) The same K_A values for $Cu^{2+}(aq)$, $Fe^{3+}(aq)$ and $Mn^{2+}(aq)$ binding to IHA and NHA confirm that sites A in IHA and NHA are chemically and structurally the same. (2) The thermodynamic affinity of site A in IHA and NHA for metals decreases in the order $Cu^{II} > Fe^{III} > Mn^{II}$. Copper(II) is a d^9 centre, while high-spin Fe^{III} and Mn^{II} are d^5 metal centres with zero ligand-field stabilization energies.[62] The ion $Fe^{3+}(aq)$ binds more strongly than $Mn^{2+}(aq)$ because of its higher charge. (3) As found for adsorption of NACs on HAs,[14,22,23] $K_A > K_B > K_C$ when more than one binding site can be identified (Table 7). (4) For the metals investigated, site B has the highest affinity for $Cu^{2+}(aq)$. The affinity of site B for $Mn^{2+}(aq)$ is too low to prevent it from being removed by brief room-temperature water washing. Binding of $Mn^{2+}(aq)$ to site B must have a smaller K_B and larger $k_{r,B}$ than for $Fe^{3+}(aq)$, otherwise we would have detected it. (5) Site C binding is not detectable for $Fe^{3+}(aq)$ and $Mn^{2+}(aq)$ with our method because $K_A > K_B > K_C$ and K_i decreases in the order $M = Cu^{2+}(aq) > Fe^{3+}(aq) > Mn^{2+}(aq)$.

More information, including K_a data for the carboxylic acid groups of GHA, IHA and NHA, use of a wider pH range and a study of temperature dependences, will be helpful in identifying the K_i data in Table 7 with specific HA metal-binding sites.

Phenylalanine and tyrosine are biochemically interconvertible,[12c] but conversion of tyrosine into dopamine [4-(2-amino-
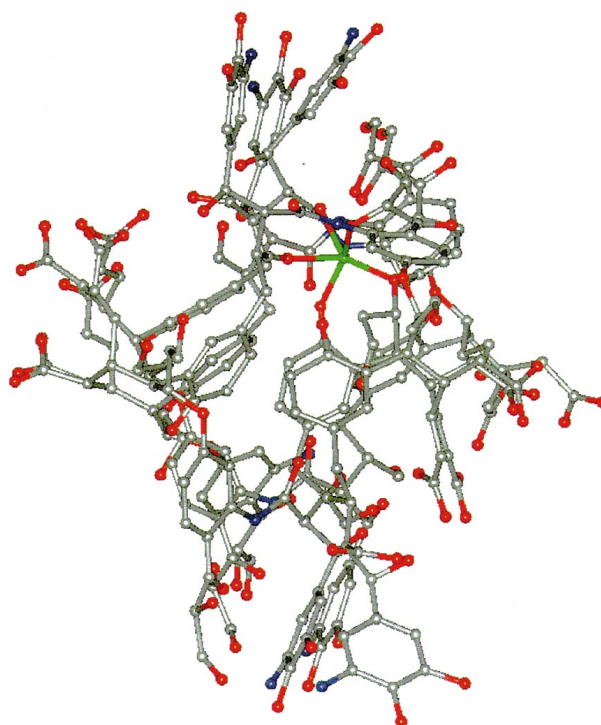

Fig. 15 Iron(III) attached to the inner lining of one turn of the HA helix.[12b] Colour code: grey, carbon; red, oxygen; blue, nitrogen; green, iron(III)

ethyl)benzene-1,2-diol] and breaking of the catechol C–C bond by tyrosinase oxygenases with a Cu_2 active site is irreversible.[63] A dicarboxylic acid group evidently is made by oxidation of a benzene ring that used to be at B in Fig. 1(a).[12c] This group seems most likely to be metal-binding site A. Other six-membered rings of the TNB could be opened in the same manner to give HAs with higher carboxylic acid contents and metal-binding capacities. The data in Table 1 indicate that this has not happened in GHA, IHA or NHA.

Our tentative assignment of site B is the mixed-ligand group at the top left of Fig. 1(a). Catechol groups are unlikely to be deprotonated in the experimental pH range 2.4–3.2. Other potential donors are the amide linkages of linked TNBs [Fig. 1(b)].

Site C is intuitively assigned as the inside of the TNB helix [Fig. 1(c)]. Fig. 15 shows Fe^{III} bound to alcohol and carbonyl groups of the helix lining.[12b] This Fe^{III} should be more easily removed by water washing than $Fe^{3+}(aq)$ bound at sites A and B, as observed for Fe^{III} and Mn^{II} (Table 7).

Free energies of binding at 20.0 °C and pH 2.4–3.2 (Table 7) were calculated from equation (6) (the symbols have their usual

$$\Delta G_i = -2.303RT \log K_i \qquad (6)$$

significance). The ΔG_i are small negative numbers like those for NAC solute adsorption[14,22–24] and are similar to each other [for example, compare ΔG_i for Cu^{2+}(aq) binding at IHA sites A, B and C]. This suggests small kinetic barriers to metal site transfer, as supported by the broad, isotropic EPR spectrum of Cu^{II}-loaded IHA at 75 K in Fig. 3(*d*). Thus, metals bound to HA appear to be mobile. Metal mobility in an HA will frustrate attempts to understand metal binding with titration experiments.[58–60] We will measure binding isotherms for other metals at different temperatures to see if v_i for a given site and metal is temperature dependent and whether the enthalpies and entropies of metal binding are correlated, as found for NAC solutes.[14,22–24] If so, then metal and solute binding by HAs has a co-operative mechanism that depends on site hydration[14,22–24] resulting from HAs' ardent love of water.

The interplay between trends $v_A < v_B < v_C$ and $K_A > K_B > K_C$ on successive HA site occupancy by a cation such as Cu^{2+}(aq) leads to a maximum metal-loading capacity MIHA = 2.3 mmol Cu^{II} g^{-1} IHA (Table 5) that is smaller than $\Sigma v_i = v_A + v_B + v_C = 5.6$ mmol Cu^{II} g^{-1} IHA (Table 7). This is because the next site, say B, can start to fill before the previous site A is full. The maximum HA capacity for a given metal at a given temperature is given by equation (7).

$$\text{MIHA} = \sum_{i=A}^{i=C} A_i = \sum_{i=A}^{i=C} K_i v_i c/(1 + K_i c) \qquad (7)$$

Metal-release rates

Environmental metal-release rates depend on rate constants, $k_{r,i}$ in equations (2) and (3). An example illustrates that metals bound to HA are not like those bound to ligands in solution. The rate constant for exchange of co-ordinated water molecules on Cu^{2+}(aq) is $\approx 2 \times 10^9$ s^{-1}.[64] Keeping the assumed D or I_d mechanism for Cu^{2+}(aq) binding by IHA for simplicity, we calculate $k_{r,B} = 2 \times 10^9/K_B \approx 6 \times 10^5$ s^{-1} from $K_B = 3.6 \times 10^3$ M^{-1} in Table 7. The predicted half-life is $0.693/6 \times 10^5 \approx 1$ µs. If dissociation of copper from site B were the slowest step, then Cu^{2+}(aq) would easily be washed out of the B sites of IHA by water. However, the A, B and C sites of IHA can be identified (Table 7) apparently because of slow diffusion of Cu^{2+}(aq) and Fe^{3+}(aq) by site hopping in the electrostricted water of water-logged IHA. Neglecting copper loss from HA particle edges, a billion or more Cu^{2+}(aq) hops would give observed half-lives of hours. Solute and solvent diffusion within functionalized polymers is understandably slow.[65] Slow rates of metal release from HAs impact directly on environmental processes and biomineralization.

Humic acid structures and biomineralization

Humic acids have important roles in biomineralization. As common plant-derived materials,[7,18] they have defined architecture and metal binding sites.[11,12] The FTIR and ^{1}H NMR spectra of purified HAs from different soils are closely similar. Many HA building block structures have been proposed. The Steelink[66] structure[11,12a] and the TNB structure in Fig. 1[12b,c] agree well with ^{1}H, ^{13}C CP MAS NMR and FTIR data. The TNB structure agrees with the formula $C_{36}H_{30}N_2O_{15}\cdot xH_2O$ ($x = 0$–15)[12b] and is predicted from rational HA biosynthesis.[12c] A biomineralization model is suggested from consideration of the TNB model of HA and common mineralization processes.[67–69]

Aluminosilicates are attached to HAs in soils[3] and plants.[7] They contain Cu and Fe in measurable quantities and other trace metals. Metal binding to HA consolidates the HA macrostructure (Fig. 6). To participate in biomineralization, HAs must serve as hosts for metals and templates for oxide construction.

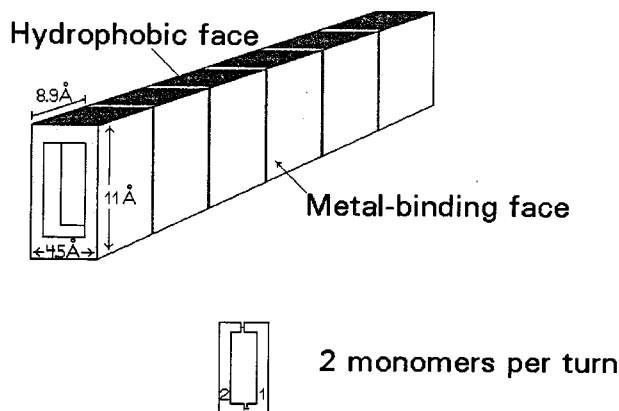Comparison of 'native', metal-free and metal-loaded HAs

Fig. 16 Schematic view of the secondary structure of an HA strand[12b]

leads to better understanding of HA–metal interactions. The EPR spectra of copper(II) centres are sensitive to their local environment. Fig. 3(*a*) and 3(*b*) show Cu^{II} in HAs that have not been treated to remove metals and minerals.[25,26] Spectral simulations of Fig. 3(*a*)–3(*c*) establish Cu^{II} in an oxide lattice that is superimposable on those for Cu^{II} in alumina or zeolite.[25] The second type of EPR spectrum [Fig. 3(*d*)] is for more mobile, less tightly bound Cu^{II}, as indicated by its broad isotropic spectrum even at 75 K. Virtually all metals in this HA sample were removed by treatment with HF/HCl, then it was reacted with Cu^{2+}(aq) from solution, washed with water and freeze dried. The parameters from EPR simulation (Fig. 3) show that Cu^{II} is bound to organic groups of HA.

Humic acid is synthesized in live or senescent plants[7,18] where metal exchange is easy. Metal binding sites of the TNB model (Fig. 1) are preserved on HA growth from HA monomers. Carboxylates are effective metal binding groups[41–46] and likely binding sites for Cu^{II} and Fe^{III}. Ions like Al^{3+} and Si^{IV} are less structurally sensitive because their binding largely results from electrostatic interactions. A wide variety of aluminosilicates associate with HAs.[3]

Fig. 16 shows the rod-like structure of a helical strand of HA.[12b] It has two parallel hydrophobic faces and two parallel hydrophilic amine-, carboxylic acid- and phenol-laden metal-binding surfaces. The rod is naturally hollow. There is no need to invoke cavities like those in primary structures of a previously proposed HA building block,[3] which seems unlikely given HAs' biochemical origin.[7,12c,18] The hollow centre is lined with alcoholic and carbonyl functional groups and normally is filled with water. The hollow interior (estimated by computer modelling to be 4×10 Å with a cross-sectional area of 40 Å^2) has selective capacity for metal cations.[12b,46]

Mineralites could form preferentially in the hollow HA interior or on its hydrophilic surfaces. The exterior has more sites with no significant steric barriers to metal binding, while the interior has a smaller number of polar sites.[12b,c]

As noted, bound metals consolidate the HA structure (Fig. 6) and reduce its solubility. Studies with chelating resins[25a] and ligands[26] demonstrate that HA solubility increases on removal of even small amounts of metals. Treatment with chelating resins[25a] probably removes metals on the rod exterior that bridge HA particles and promote HA aggregation. We know that tiron® removes at least two forms of bound iron(III) and is a more effective demetallator and demineralizer of HAs than Chelex® resin;[25a,26] Tiron® can traverse the rod interior and evidently removes cations from the HA surface and its hollow centre.

The HA secondary structural alignment of functional groups with regular 9 Å spacing on parallel metal-binding surfaces (Fig. 16)[12b] offers periodic nucleation sites for mineral crystal propagation. Biomineralization likely begins in the plant with metal exchange[7] but is completed in the soil. Fig. 17 shows an
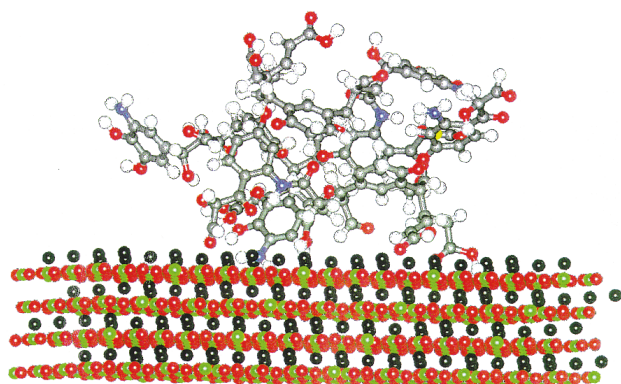
Fig. 17 A tetramer made from four lowest-energy TNB building blocks [Fig. 1(*a*)] interacts through its amine and carboxylate functional groups with an aluminosilicate surface. Colour code: black, carbon; red, oxygen; blue, nitrogen; green, silicon; light green, aluminum [12b]
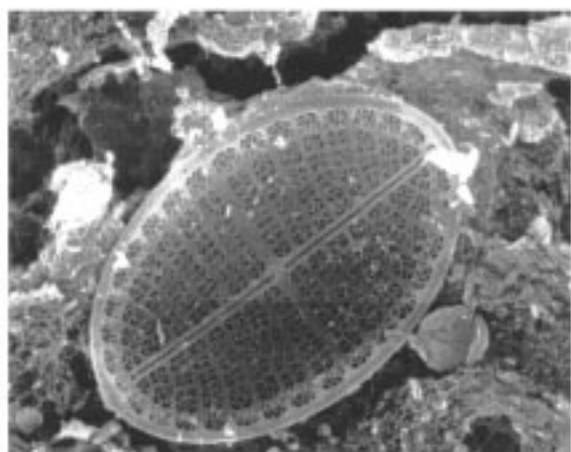

Fig. 18 A diatom found on the surface of HA isolated from the alga *Pilayella littoralis* with the methods in Scheme 1 and refs. 28–30 [7,18]

HA tetramer bound to an aluminosilicate surface, which is the culmination of this process and the beginning of new HA propagation. We found the diatom in Fig. 18 on the surface of a sample of HA isolated from the marine alga *Pilayella litoralis*.[7,18]

Conclusion

The numbers of nearest-atom neighbours of Cu^{II}, Fe^{III} and Mn^{II} in the tight metal-binding sites of solid GHA, IHA and NHA are four, six (probably with distorted geometry) and six (undistorted), respectively. Data for tight binding of Cu^{II}, Fe^{III} and Mn^{II} sites i = A, B, and C in solid IHA and NHA at 20.0 °C fit the Langmuir model. The stoichiometric site capacities v_i and equilibrium binding constants K_i are independent of pH in the range 2.4–3.2 with $[M]_{total}$ = 0.18–25.8 mM. Comparisons of v_i and K_i data indicate that sites A of IHA and NHA are identical. Spectral evidence is consistent with carboxylate as site A. Mixed ligands probably constitute site B, and site C is tentatively assigned as the interior of the HA helix. Binding free energies and EPR evidence indicate that Cu^{2+}(aq), Fe^{3+}(aq) and Mn^{2+}(aq) rapidly transfer between specific HA binding sites. This affects the rates of metal release from HAs to water and minerals.

Acknowledgements

References

1 W. Ziechmann, *Humic Substances*, BI Wissenchaftsverlag, Mannheim, 1993.
2 R. Beckett, in *Surface and Colloid Chemistry in Natural Water and Water Treatment*, ed. R. Beckett, Plenum, New York, 1990, pp. 3–20.
3 H.-R. Schulten and M. Schnitzer, *Naturwissenschaften*, 1995, **82**, 487; *Soil Sci.*, 1997, **162**, 115 and refs. therein; H.-R. Schulten and P. Leinweber, *J. Anal. Appl. Pyrolysis*, 1996, **38**, 1 and refs. therein.
4 A. Piccolo, S. Nardi and G. Concheri, *Chemosphere*, 1996, **33**, 595; *Eur. J. Soil Sci.*, 1996, **47**, 319.
5 P. MacCarthy, C. E. Clapp, R. L. Malcolm and R. R. Bloom, *Humic Substances in Soil and Crop Sciences: Selected Readings*, American Society of Agronomy, Madison, WI, 1990.
6 *Humic Substances in the Global Environment: Implications for Human Health*, eds. N. Senesi and T. M. Miano, Elsevier, Amsterdam, 1994.
7 E. A. Ghabbour, A. H. Khairy, D. P. Cheney, V. Gross, G. Davies, T. R. Gilbert and X. Zhang, *J. Appl. Phycol.*, 1994, **6**, 459.
8 N. Senesi, in ref. 6, pp. 3–43.
9 R. Österberg, *Proc. 8th Mtg. IHSS*, in the press.
10 E. Tombaćz, J. A. Rice and S. Ren, *Proc. 8th Mtg. IHSS*, in the press.
11 G. Davies, E. A. Ghabbour, S. A. Jansen and J. Varnum, in *Advanced New Materials and Emerging New Technologies*, eds. P. N. Prasad, J. E. Mark and T. J. Fai, Plenum, New York, 1995, pp. 677–685 and refs. therein.
12 (*a*) S. A. Jansen, M. Malaty, S. Nwabara, E. Johnson, E. A. Ghabbour, G. Davies and J. M. Varnum, *Mater. Sci. Eng.*, 1996, **C3**, 175; (*b*) S. A. Jansen, L. T. Sein, jun., G. Davies and E. A. Ghabbour, unpublished work; (*c*) L. T. Sein, jun. and S. A. Jansen, unpublished work.
13 R. L. Wershaw, *J. Contamin. Hydrol.*, 1986, **1**, 29; *US Geological Survey Water-Supply Paper* 2410, 1994; *Environ. Sci. Technol.*, 1993, **27**, 814.
14 G. Davies, E. A. Ghabbour, A. H. Khairy and H. Z. Ibrahim, *J. Phys. Chem.*, 1997, **101B**, 3328 and refs. therein.
15 M. H. B. Hayes and F. L. Himes, in *Interactions of Soil Minerals with Natural Organics and Microbes*, eds. P. M. Huang and M. Schnitzer, SSSA Special Publication No. 17, Soil Science Society of America, Madison, WI, 1986, pp. 103–159.
16 (*a*) *Humic Substances II: In Search of Structure*, eds. M. H. B. Hayes, P. MacCarthy, R. L. Malcolm and R. S. Swift, Wiley-Interscience, New York, 1989; (*b*) *Humic Substances in the Environment*, eds. F. H. Frimmel and R. F. Christman, Wiley, New York, 1989.
17 G. R. Aiken, D. M. McKnight, R. L. Wershaw and P. MacCarthy, in *Humic Substances in Soil, Sediment and Water*, eds. G. R. Aiken, D. M. McKnight, R. L. Wershaw and P. MacCarthy, Wiley-Interscience, New York, 1985.
18 A. Radwan, G. Davies, A. Fataftah, E. A. Ghabbour, S. A. Jansen and R. J. Wiley, *J. Appl. Phycol.*, 1997, **8**, 553.
19 A. Radwan, R. J. Willey and G. Davies, *J. Appl. Phycol.*, in the press.
20 B. Xing, J. J. Pignatello and B. Gigliotti, *Environ. Sci. Technol.*, 1996, **30**, 2432 and refs. therein.
21 C. T. Chiou, J. F. Lee and S. A. Boyd, *Environ. Sci. Technol.*, 1990, **24**, 1164; C. T. Chiou, D. W. Rutherford and M. Manes, *Environ. Sci. Technol.*, 1993, **27**, 1587.
22 A. H. Khairy, G. Davies, H. Z. Ibrahim and E. A. Ghabbour, *J. Phys. Chem.*, 1996, **100**, 2410.
23 A. H. Khairy, G. Davies, H. Z. Ibrahim and E. A. Ghabbour, *J. Phys. Chem.*, 1996, **100**, 2417.

24 E. A. Ghabbour, G. Davies, A. Fataftah, N. K. Ghali, M. E. Goodwillie, S. A. Jansen and N. A. Smith, *J. Phys. Chem.*, in the press.

25 (*a*) S. A. Jansen, M. D. Paciolla, E. A. Ghabbour, G. Davies and J. M. Varnum, *Mater. Sci. Eng.*, 1996, **C4**, 181; (*b*) T. M. Abdel-Fattah, G. Davies, B. V. Romanovsky, O. L. Shakhanovskaya, A. N. Larin, S. A. Jansen and M. J. Palmieri, *Catal. Today*, 1997, **33**, 313.

26 G. Davies, A. Fataftah, A. Cherkasskiy, A. Radwan, S. A. Jansen, M. D. Paciolla and E. A. Ghabbour, *Proc. 8th IHSS Mtg.*, in the press.

27 M. Schnitzer, *Proc. Int. Mtg. ln Humic Subst.*, *Wageningen*, 1972, 293.

28 F. Scheffer, W. Ziechmann and G. Pawelke, *Z. Pflanzenernaehr. Dueng. Bodenkd.*, 1960, **90**, 58.

29 R. H. Pierce, jun. and G. T. Felbeck, jun., *Proc. Int. Mtg. Humic Substances, Niewersluis*, 1972, 217.

30 J. N. C. Whyte, in *Experimental phycology: A laboratory manual*, eds. C. S. Lobban, D. J. Chapman and B. P. Kremer, Cambridge University Press, New York, 1988, pp. 168–173.

31 B. E. Watt, T. M. Hayes, M. H. B. Hayes, B. T. Price, R. L. Malcolm and P. Jakeman, in *Humic Substances and Organic Matter in Soil and Water Environments*, eds. C. E. Clapp, M. H. B. Hayes, N. Senesi and S. M. Griffiths, International Humic Substances Society, St. Paul, MN, 1996, pp. 81–91.

32 D. L. Sparks, *Environmental Soil Chemistry*. Academic Press, San Diego, 1995.

33 F. J. Stevenson, *Humus Chemistry: Genesis, Composition, Reactions*, Wiley, New York, 2nd edn., 1994.

34 B. Xing, W. B. McGill and M. J. Dudas, *Environ. Sci. Technol.*, 1994, **28**, 1929.

35 M. A. Wilson, *NMR Techniques and Application in Geochemistry and Soil Chemistry*, Pergamon, Oxford, 1987; *Soil Analysis: Modern Instrumental Techniques*, ed. K. A. Smith, Marcel Dekker, New York, 2nd edn., 1991, pp. 601–645.

36 Z. Chen and S. Pawluk, *Geoderma*, 1995, **65**, 173.

37 R. L. Cook, C. H. Langford, R. Yamdagni and C. M. Preston, *Anal. Chem.*, 1996, **68**, 3979.

38 N. D. Chasteen, R. J. DeKoch, B. R. Rogers and M. W. Hanna, *J. Am. Chem. Soc.*, 1973, **95**, 4.

39 *Principles, Applications and Techniques of EXAFS, SEXAFS and XANES Spectroscopy*, eds. D. Koningsberger and R. Prins, Wiley, New York, 1988.

40 Y. Chen, N. Senesi and M. Schnitzer, *Geoderma*, 1978, **20**, 87.

41 N. Senesi and G. Calderoni, *Org. Geochem.*, 1988, **13**, 1145.

42 N. Senesi, G. Sposito, G. R. Bradford and K. M. Holtzlaw, *Water, Air, Soil Pollut.*, 1991, **53**, 409.

43 N. Senesi, S. M. Griffith, M. Schnitzer and M. G. Townsend, *Geochim. Cosmochim. Acta*, 1977, **41**, 969.

44 M. B. McBride, *Soil Sci.*, 1978, **126**, 200.

45 N. Senesi, *Trans. World Congress Soil Sci.*, 1994, **39**, 384.

46 A. Fataftah, Doctoral dissertation, Northeastern University, 1997.

47 S. A. Jansen, J. M. Varnum, S. Kolla, M. D. Paciolla, A. Radwan, E. A. Ghabbour and G. Davies, *Proc. 8th IHSS Mtg.*, in the press.

48 J. A. Leenheer, R. L. Wershaw, G. K. Brown and M. M. Reddy, unpublished work.

49 T. M. Tranquader, S. M. Heald and A. R. Moodenbaugh, *Phys. Rev. B*, 1987, **36**, 5263.

50 E. E. Alp, G. K. Shenoy, D. G. Hinks, D. W. Capone II, L. Soderholm, H.-B. Schuttler, J. Guo, D. E. Ellis, P. A. Montano and M. Ramanathan, *Phys. Rev. B*, 1987, **35**, 7199.

51 J. E. Hahn, R. A. Scott, K. O. Hodgson, S. Doniach, S. Desjardins and E. I. Solomon, *Chem. Phys. Lett.*, 1982, **88**, 595.

52 J. N. van Niekerk and F. R. L. Schoening, *Acta Crystallogr.*, 1953, **6**, 227.

53 J. J. Rehr, J. Mustre de Leon, S. I. Sabinsky and R. C. Albers, *J. Am. Chem. Soc.*, 1991, **113**, 5136.

54 J. Zhao, F. E. Huggins, Z. Feng, F. Lu, N. Shah and G. P. Huffmann, *J. Catal.*, 1993, **143**, 499.

55 E. F. Bertraut, Tran Qui Duc, P. Burlet, P. Burlet, M. Thomas and J. M. Moreau, *Acta Crystallogr.*, 1974, **30**, 2234.

56 J. Silver, in *Chemistry of Iron*, ed. J. Silver, Chapman and Hall, Glasgow, 1993.

57 C. F. Baes, jun. and R. E. Messmer, *The hydrolysis of cations*, Wiley, New York, 1976, chs. 10 and 12.

58 T. Qiang, S. Xiao-Quan and N. Zhe-Ming, *Anal. Chem.*, 1994, **66**, 3562.

59 E. P. Anterberg and C. M. G. van der Berg, *Anal. Chim. Acta*, 1994, **291**, 213 and refs. therein.

60 J. Ephaim and J. A. Marinsky, *Environ. Sci. Technol.*, 1986, **20**, 367 and refs. therein.

61 R. G. Wilkins, *Kinetics and Mechanism of Reactions of Transition Metal Complexes*, VCH, New York, 2nd edn., 1991.

62 J. E. Huheey, *Inorganic Chemistry*, Harper and Row, New York, 3rd edn., 1983, p. 382.

63 E. I. Solomon, U. M. Sundaram and T. E. Machonkin, *Chem. Rev.*, 1996, **96**, 2563.

64 L. Helm, S. F. Lincoln, A. E. Merbach and D. Zbinden, *Inorg. Chem.*, 1986, **25**, 2550; L. S. W. L. Sokol, T. B. Fink and D. B. Rorabacher, *Inorg. Chem.*, 1980, **19**, 1263.

65 C. E. Rogers, in *The Physics and Chemistry of the Organic Solid State*, eds. D. Fox, M. M. Labes and A. R. Weissberger, Interscience, New York, 1965, ch. 6; W. R. Vieth, *Diffusion in and through Polymers*, Oxford University Press, Oxford, 1991.

66 C. Steelink, in ref. 17, pp. 457–476.

67 H. A. Lowenstein, *On Biomineralization*, Oxford University Press, New York, 1989.

68 K. Simkiss and K. M. Wilbur, *Biomineralization*, Academic Press, San Diego, 1989.

69 G. Sposito, *The Chemistry of Soils*, Oxford University Press, New York, 1989.